Qualitative Geochemical Analysis of the 2004 Indian Ocean Giant Tsunami Deposits Excavated at Seungko Mulat Located in Aceh Besar of Indonesia Using Laser-Induced Breakdown Spectroscopy

Rara Mitaphonna[1], Muliadi Ramli[2], Nazli Ismail[3], and Nasrullah Idris[3*]

[1]*Graduate School of Mathematics and Applied Sciences, Universitas Syiah Kuala, Banda Aceh 23111, Indonesia*

[2]*Department of Chemistry, Faculty of Mathematics and Natural Sciences, Universitas Syiah Kuala, Banda Aceh 23111, Indonesia*

[3]*Department of Physics, Faculty of Mathematics and Natural Sciences, Universitas Syiah Kuala, Banda Aceh 23111, Indonesia*

** **Corresponding author:***

email: nasrullah.idris@usk.ac.id

Received: August 16, 2023
Accepted: February 27, 2024

DOI: 10.22146/ijc.88086

Abstract: *Laser-induced breakdown spectroscopy (LIBS) was employed to characterize the geochemical signatures layer by layer of 2004 Indian Ocean tsunami deposits in Seungko Mulat Village, Aceh Province, Indonesia. In the LIBS experimental setup, a Nd-YAG laser beam is directed towards the deposit samples, and the resulting atomic emission lines from the laser-induced plasma are captured using a spectrometer. Our analysis reveals terrestrial indicators (Fe), heavy metals (Cu, Cr, Co, Cd), and increased emission intensity of Mg, Ca, Al, K, Si, Ba, N, and O in the 2004 Indian Ocean tsunami layers. The emission intensity ratios of several elements in the 2004 Indian Ocean tsunami deposit layers, namely Ca/Ti, Si/Ti, and K/Ti, unveil notable disparities among the elements evaluated. This indicates the possibility of utilizing these ratios as reliable geochemical markers to differentiate the layer by layer of tsunami deposits. LIBS surpasses XRF in detecting nearly all elements simultaneously and identifying both light elements and specific heavy metals (Ba, Cu, Cr, Co, Cd, Pb, Ni, V, W), exceeding XRF's detection capabilities. This study emphasizes the effectiveness of LIBS as an advanced optical technique, offering speed and promise in analyzing layer-by-layer geochemical markers of the 2004 Indian Ocean tsunami deposits in Seungko Mulat Village.*

Keywords: *LIBS; chemical profile; 2004 Indian Ocean tsunami; tsunami deposit layers; Aceh*

■ INTRODUCTION

On December 26th 2004, a momentous event unfolded as a cataclysmic earthquake, registering 9.1 on the Richter scale, shook the oceanic crust beneath Sumatra Island, Indonesia. This seismic upheaval, triggered by the subduction of a dense marine plate beneath a lighter continental crust, led to a profound elevation of the ocean floor, reaching staggering heights of up to 40 m. Consequently, a catastrophic Indian Ocean tsunami was unleashed. The initial impact of the tsunami's immense force was keenly felt along coastal areas, including the capital city of Aceh Province. The 2004 Indian Ocean tsunami resulted in 230,000 deaths and transformed a once-thriving city into a scene of ruins and debris along the Indian Ocean coastline [1-2]. This indiscriminate fury caused an overwhelming loss of life and inflicted widespread devastation upon human settlements and pristine natural environments in its submerged path [3]. The significant advancements in geodesy and seismology have brought forth valuable insights into rupture patterns associated with major earthquakes. However, the 2004 Indian Ocean mega-disaster highlights the significant challenges in our understanding of seismological and oceanic upheavals [4]. The ongoing pursuit of scientific knowledge in these realms remains indispensable in an unyielding commitment to safeguarding vulnerable coastal communities and mitigating the potential impact of future seismic.

In the wake of the catastrophic tsunami waves, coastal systems and terrestrial regions underwent significant sedimentation, which gave rise to the formation of tsunami deposits. These sedimentary assemblages hold immense significance as invaluable geological archives for researchers and emergency planners grappling with disaster mitigation [5]. Tsunami deposits serve as compelling testimony, providing historical documentation of past tsunami inundation events and facilitating precise assessments of tsunami recurrence and frequency [6].

Numerous extensive investigations have been undertaken to explore diverse constituents present within tsunami deposits using a wide range of scientific indicators, including geological, sedimentological, paleontological, and micro-paleontological [7-8]. However, when it comes to applying these indicators in vast areas severely impacted by tsunamis, challenges arise. The behavior of tsunami waves near the inundation limit, where their velocity diminishes, leads to reduced carrying capacity, thereby impeding the transportation of larger, visually detectable particles [9]. To surmount this limitation, researchers have previously devised geochemical indicators to study the chemical imprints within tsunami deposits both from contemporary and prehistoric occurrences. Throughout the preceding three decades, there has been a substantial evolution in geochemical methodologies, propelling them to the forefront of research as promising and highly responsive tools for identifying tsunami events. In recent studies, extensive investigations have provided compelling evidence supporting the preservation of geochemical signatures within tsunami deposits for extended geological timescales spanning several centuries, and even imperceptible deposits hold significant potential for yielding valuable insights into past tsunami events [10]. The pivotal role of organic and inorganic geochemical markers lies in their ability to distinguish between terrestrial and marine materials, thereby unravelling the sources of chemical elements present within the tsunami context [11-12].

Exhaustive scientific investigations have been undertaken after the catastrophic 2004 event to investigate the characteristics of tsunami sediments in severely impacted regions, including India, Thailand, and notably Aceh Province in Indonesia [13-15]. These inquiries have rendered profound insights into the intricate composition of tsunami deposits particularly focusing on the ubiquitous presence of salinity, metallic, and heavy metal constituents. A qualitative analysis conducted in Aceh Province nearly a decade after the tsunami revealed noticeable salt element differences between the tsunami-influenced soil samples and the adjacent undisturbed soil. The discernible escalation of salt elements encompassing Ca, Mg, K, and Na in tsunami-affected soil offers compelling evidence of their deposition during the cataclysmic tsunami event [16-17]. Additionally, in soils severely impacted by the tsunami in Aceh Province, a discernible elevation in terrestrial markers (Ti, Fe) and marine carbonates (Mg) has been observed [2]. As time progresses, differentiating between terrestrial and marine geochemical markers within tsunami deposits poses an escalating challenge owing to substantial fluctuations in elemental concentrations that tend to obscure clear signals. To address this formidable obstacle, researchers have extensively employed elemental concentration ratios as a potent analytical tool for discerning tsunami-affected areas. By examining these ratios, researchers gain invaluable insights into the distinctive geochemical characteristics of tsunami deposits, thus facilitating the precise identification and delineation of inundated regions [18].

Numerous analytical methodologies have been employed to accurately ascertain and quantify the chemical constituents within the specimens. These techniques encompass atomic fluorescence spectrometry [19], flame atomic absorption spectrometry [20], inductively coupled plasma-mass spectroscopy [21], and X-ray fluorescence [22-23]. However, these instruments typically require sample preparation, leading to time-consuming analysis procedures and increased energy consumption, which may not be suitable for rapid and *in situ* analyses.

In contrast, the laser-induced breakdown spectroscopy (LIBS) technique offers a rapid and efficient approach to multi-elemental analysis, streamlining the analytical process, and it is esteemed for

its dependable elemental analysis capabilities due to its intrinsic ease of use, versatility, sensitivity, and specificity [24]. Unlike many other methods, LIBS stands out for its capability to access the entire periodic table of elements. As a result, this technique allows for the precise measurement of the key constituents of all biological and geological materials, including the non-metals hydrogen (H), carbon (C), nitrogen (N), and oxygen (O) [25]. Another significant advantage of LIBS is that this analytical technique not only offers information regarding the elemental composition of the sample but also provides access, to some degree, to molecular information [26]. Indeed, while there have been numerous investigations exploring LIBS soil analysis in agriculture and geographic distribution [27-30], the novelty of this research lies in the unique application of LIBS analysis to examine layer-by-layer chemical profiles of tsunami sediments on the Aceh Besar Regency coastal area, Aceh Province, Indonesia. We also employed a combination of LIBS analysis and principal component analysis (PCA) to discern distinctions between samples from tsunami deposits and non-tsunami deposits, thus facilitating differential investigations into the elemental composition and soil characteristics, providing invaluable insights into the geological history. To our understanding, this study marks the pioneering application of the LIBS-PCA approach in classifying tsunami deposit samples.

■ EXPERIMENTAL SECTION

Materials

The 2004 Indian Ocean tsunami deposit samples were collected from Seungko Mulat Village, which was profoundly affected by the catastrophic 2004 Indian Ocean tsunami. Positioned approximately 44 km from Aceh Province's capital city, Seungko Mulat Village experienced the full force of the tsunami's impact owing to its direct exposure to the Indian Ocean (Fig. 1). Seungko Mulat Village was chosen as a highly promising site for tsunami research based on its coastal morphology and the documented occurrences of land uplift and subsidence events linked to tectonic activity both pre- and post-earthquakes. The village met the essential requisites as a viable tsunami deposit area due to its flat topography, slight depression, and minimal disturbances from regular coastal currents or human activities [31]. The collection of tsunami deposit samples was conducted in February 2022, nearly two decades after the cataclysmic tsunami struck the region. We conducted the sampling in swampy regions situated approximately 1.6 km inland and at a slightly lower altitude of 0.2 m relative to the sea surface. Before the tsunami disaster, this area primarily functioned as a rice field. However, the disaster rendered it barren and untapped for a considerable period.

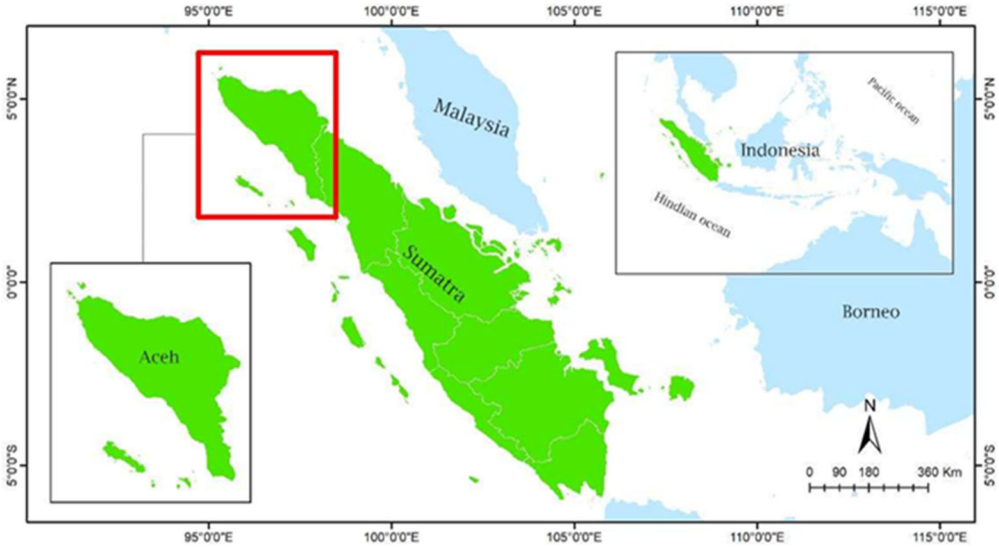

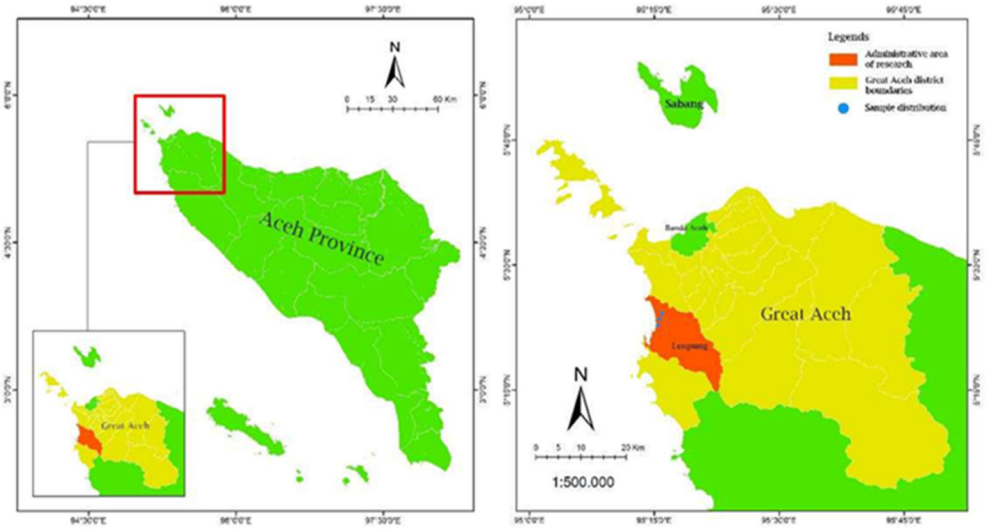

Fig 1. The sampling locations of the 2004 Indian Ocean tsunami deposits were designated in Seungko Mulat Village, Aceh Besar Regency, Aceh Province, Indonesia. These locations were visually marked using yellow indicators, while the precise sampling points were distinguished by red highlights

To undertake the collection of samples, we utilized a hand auger, a specialized tool comprising sharp, cylindrical iron pieces at both ends, with a rotation mechanism atop the hand drill. The auger was driven vertically into the ground until it encountered a firm, unyielding stratum. We employed the Troels-Smith classification method to discern and categorize the acquired tsunami deposits. Each sediment layer was inspected and evaluated through tactile perception to ascertain its distinct nature and elemental components. The sample preparation procedure initiates with the removal of all organic material, followed by drying the sample in an oven at 105 °C for 1 h. Subsequently, the dried samples undergo crushing and sieving using a 200 mesh sieve to achieve a uniform particle size distribution. Then, the sample is compacted into pellet form using a hydraulic press machine applying a force of 5 tons. This process yields pellets measuring 0.7 cm in width and 0.6 cm in thickness.

Instrumentation

The experimental setup is depicted in Fig. 2. A 1064 nm Nd:YAG laser serves as the excitation source for plasma generation initiation. The laser, featuring a pulse duration of 8 ns and a delay time of 2 μs, operates at an energy of 56 mJ/pulse and is collimated onto the sample surface through a lens with a focal length of 17 cm. In LIBS, a high-energy laser pulse is directed to achieve a focal point on the sample's surface, thereby generating

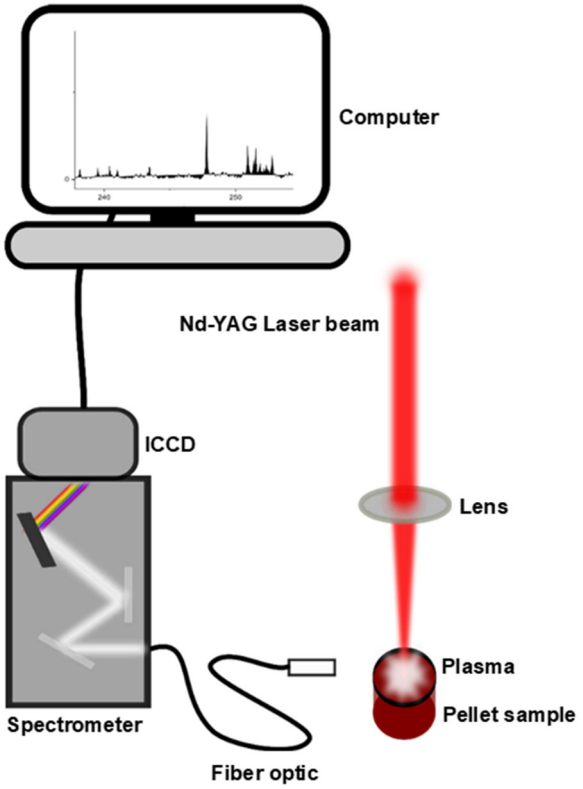

Fig 2. The experimental configuration of the LIBS system

an intense and radiant plasma plume composed of ions, electrons, and excited atoms and molecules. Following the cooling of the laser-induced plasma, it gives rise to characteristic atomic spectra from neutral and ionized species, serving as unique signatures that unveil the elemental constitution of the sample. To capture and analyze these emissions, the plasma is channeled towards a spectrograph outfitted with an intensified charge-coupled device (ICCD) camera system. The ICCD camera served to capture the optical signals that entered the spectrometer (Andor, iStar 320 T), subsequently transforming them into digital signals. The entire function of the OMA system was steered via the ANDOR SOLIS software installed on a dedicated computer. The plasma's emitted spectrum was then projected on a monitor and recorded for subsequent scrutiny of the accumulated data. During the data analysis phase, spectral emission lines were identified and confirmed by comparing the observed wavelengths of emission lines with those registered in the National Institute for Science and Technology (NIST) database. Before commencing the LIBS analysis, we evaluated the delay time and laser energy to determine the optimal experimental conditions. This calculation was conducted to ensure precise timing and laser energy levels, both of which are essential for achieving accurate measurements.

Procedure

Grain size analysis

The assessment of grain size was executed with a respected Malvern MS 3000 laser particle size analyzer known for its capacity to evaluate grain sizes as large as 1800 µm. The samples were treated by dissolving them in a 30% hydrogen peroxide (H_2O_2) solution to eliminate organic components, while a 10% hydrochloric acid (HCl) solution was utilized to remove carbonate content. Preservation of the samples involved immersing them in a solution of sodium hexametaphosphate ($(NaPO_3)_6$) at room temperature for 24 h to maintain stability. Subsequently, the samples undergo rinsing with distilled water until all dirt and contaminants are thoroughly removed. Following this, the grain size characteristics of each sample are analyzed using the logarithmic graphic method facilitated by GRADISTAT software [32]. This examination encompasses various factors, such as average grain size, skewness, sorting, kurtosis, and the relative proportions of sand, clay, and silt [33].

PCA

We utilized a straightforward chemometric technique known as PCA. This method serves to simplify the complexity of extensive datasets derived from a wide array of LIBS spectral data. PCA is a popular method for statistically evaluating LIBS data due to its high efficiency in discerning patterns and organizing groups of LIBS spectral data, while simultaneously reducing data dimensionality. Moreover, PCA offers the added advantage of identifying key emissions in the LIBS spectrum that significantly contribute to the discrimination process. We conducted PCA using two components to represent the extracted LIBS spectrum. This innovative research represents a paradigm shift in the application of the LIBS-PCA technique for classifying tsunami deposit samples, thus opening new avenues in this burgeoning research domain.

■ RESULTS AND DISCUSSION

Characteristics of Tsunami Deposit

The study area encompasses a stratigraphic profile and grain size distribution of sediment in Seungko Mulat Village, located along a coastline with a broad contour featuring gentle slopes. The geological composition primarily comprises youthful Holocene formations, including alluvial and coastal deposits. Alluvial deposits consist of clay, silt, sand, gravel, and cobbles, while coastal deposits are characterized by loosely arranged sand exhibiting moderate to good sorting. Noteworthy morphological features, such as beach ridges and swales, were observed during field inspections in the research area. Our designated sampling point was chosen within the basins situated between these ridges. Throughout our study, we executed drilling operations delving into the ground to a depth exceeding 1 m, uncovering a sequence of soil layers exhibiting striking color variations. These distinct layers comprised a topsoil layer, a tsunami deposit layer, and a paleo soil layer. Utilizing megascopic analysis, we successfully identified the 2004 Indian Ocean tsunami

deposits at a specific depth range of 4 to 24 cm (Fig. 3). Remarkably, the tsunami deposit layer showcased unique and discernible characteristics, setting it apart from the adjacent layers above and below.

The uppermost layer (0–4 cm) consists of fine-textured yellowish-brown sand with an average grain diameter of 3.394 ϕ, predominantly comprising 94.9% sand and 5.1% silt and exhibiting a well-sorted nature (0.354 ϕ). The kurtosis value indicates a leptokurtic curve (1.183 ϕ) (Fig. 4). A distinct boundary is observed, sharply separating this layer from the underlying strata. Within this layer, vestiges of vegetation, including twigs, stems, and roots, are found, denoting the commencement of soil formation after the 2004 Indian Ocean tsunami. Over several months following the tsunami event, the sediment deposited by the tsunami

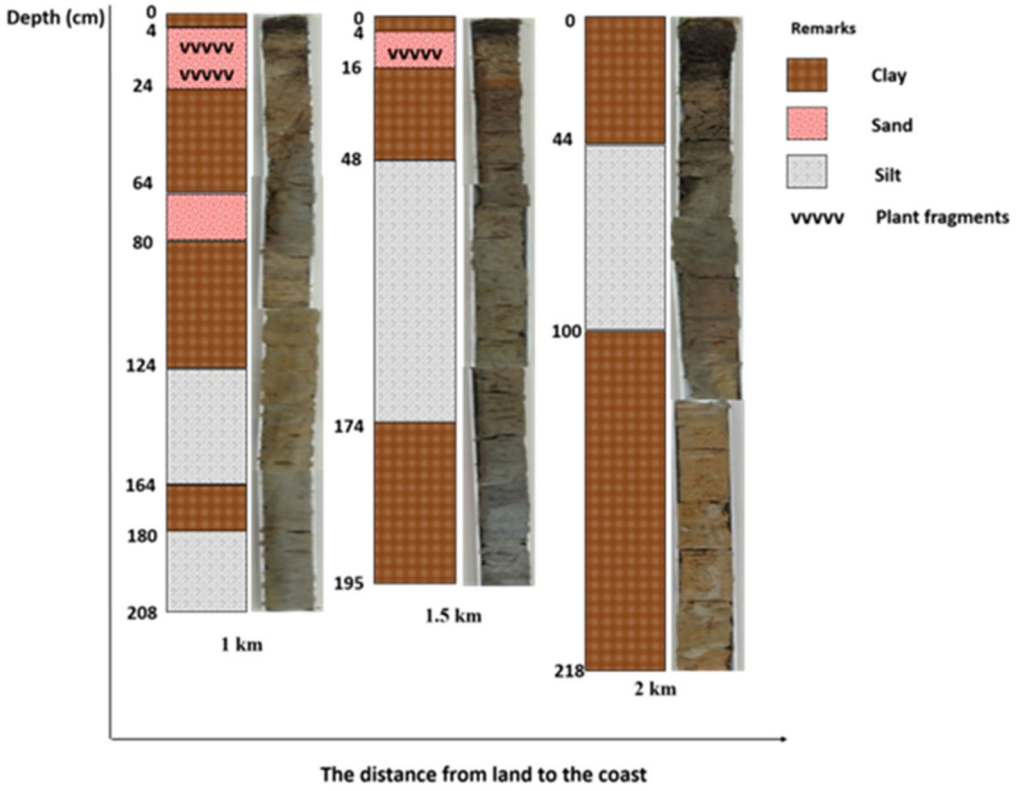

Fig 3. The stratigraphic profiles of deposit samples were collected from various points at Seungko Mulat Village

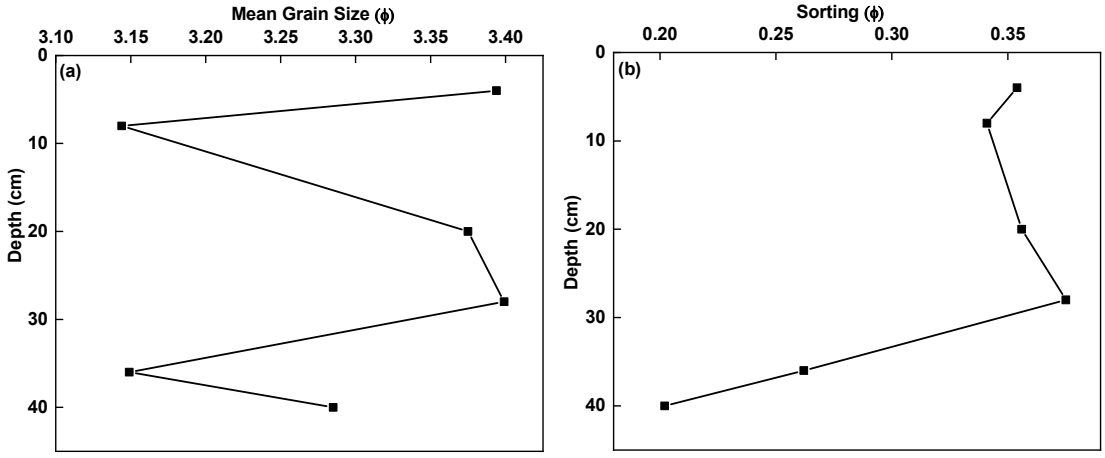

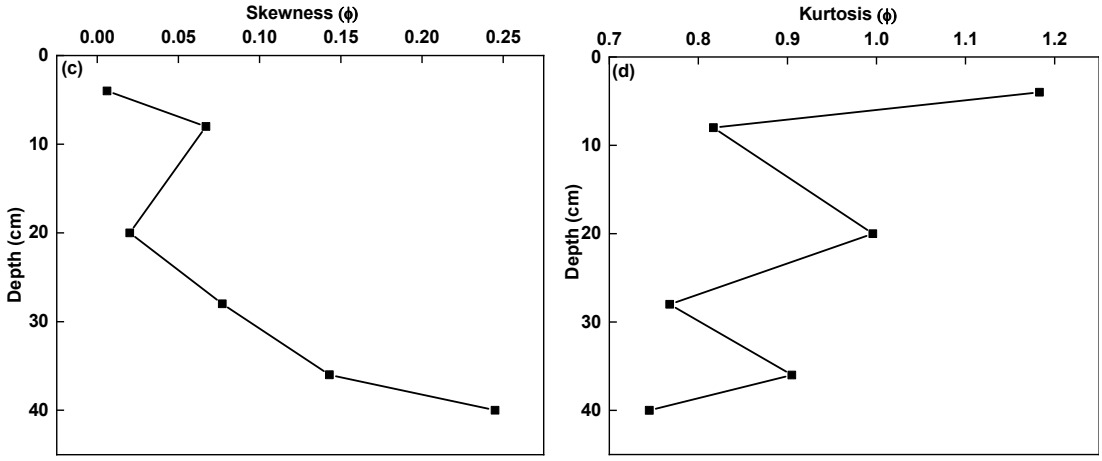

Fig 4. The grain size parameters of deposit samples (a) mean grain size, (b) sorting, (c) skewness, and (d) kurtosis

facilitated the growth of vegetation, contributing to the establishment of new soil.

Based on the observed characteristics, we can discern the presence of layers deposited during the 2004 Indian Ocean tsunami disaster beneath the topsoil layer. Tsunami sediments are typically discernible based on multiple criteria, encompassing deposition on subsided soil as a consequence of co-seismic activity, larger grain sizes compared to neighboring deposits due to elevated depositional energy, finer grain sizes in inland regions, the thickness of the sand layer, the existence of reworked fragments and the evidence of shell material from marine sediment sources [34-36]. The sediment properties yield valuable insights into tsunami hydrodynamics and enhance our comprehension of tsunami magnitudes. The sedimentary layers related to the 2004 Indian Ocean tsunami in this study were identified as a layer of grey sand, approximately 20 cm thick, covering paleo soils (Fig. 3). In various locations, laminated silt layers and decaying plant remains, such as roots and stems, were found. This observation aligns with the co-seismic subsidence theory proposed by Atwater and Hemphill-Haley. Before the earthquake, the land was uplifted and covered with trees. However, following the earthquake and tsunami, the land subsided and became inundated with water, resulting in the formation of swamps and subsequent deposition of tidal mud. The tsunami deposit layer exhibits clear boundaries with the layers above and below it. The sharp interface at the bottom of the tsunami deposit layer indicates a sudden and rapid change in sedimentation patterns. In contrast, the upper contact demonstrates a gradual and comparatively slower deposition process following the tsunami event. Another notable feature of the identified tsunami deposits in this study is their well-defined normal gradation, where the grain size of the sediment decreases progressively from the base to the top of the deposit. The tsunami deposit layer predominantly comprises medium to fine-grained sand, displaying a polymodal distribution and a well-sorted texture. The mean grain size increases from 3.144 to 3.399 ϕ with increasing depth (Fig. 4), indicating variations in the velocity of the tsunami waves during the run-up and backwash phases. The fast run-up flow results in coarser-grained deposits at the bottom of the tsunami bed, while the slower backwash flow leads to the deposition of fine-grained sediments. Due to the diverse range of grain sizes, the tsunami deposit layer exhibits kurtosis values associated with both mesokurtic and leptokurtic curves.

Furthermore, below the layer of tsunami sediment, there is a paleo soil layer composed of sandy silt that exhibits a bimodal distribution with a value of 0.202 ϕ (Fig. 4). In certain areas, this layer exhibits a bluish-grey color, while in others, it appears brownish-grey. The soil in this layer has a sticky consistency, making it challenging to penetrate with a hand drill. This phenomenon is hypothesized to arise from the reduction-oxidation reaction of the chemical element iron in the soil. As we dig deeper, a higher concentration of organic material, including shell fragments, becomes evident.

Optimization of Delay Time

Optimizing laser parameters is an essential process in obtaining precise and dependable outcomes during LIBS analysis. It is necessary to fine-tune various critical laser parameters to enhance the analytical capabilities of this technique. In the process of LIBS analysis, an intense pulsed laser is used instead to impart a substantial amount of energy onto the sample, thereby inducing the formation of a plasma at its surface. The laser-induced plasma comprises atoms in an excited state, molecules in an excited state, atoms that have been ionized, molecules that have been ionized, and a swarm of electrons. Consequently, these energized and ionized entities release emissions, resulting in a wide-ranging emission spectrum. In the early stages of continuum emission, conducting a thorough material analysis is impractical. However, as the plasma cools, a substantial portion of the energized and ionized entities undergo recombination. Eventually, a distinct stage is reached where only a small number of neutral atoms and ions persist in the excited state. It is during this phase that the emissions from these excited species become more distinct and specific, allowing for enhanced observation and analysis. Selecting an appropriate time delay is crucial for the successful completion of LIBS spectral analysis as it involves utilizing a camera for both quantitative and qualitative analysis of the spectra. In reality, different elements may require different optimal time delays. To ascertain the ideal time delay, we utilize a specific characteristic wavelength known as the Ca II line at 396.84 nm within the wavelength range of 390–400 nm. The signal intensity is recorded for various time delays corresponding to each line. The optimization of delay time is performed within the range of 0.1 to 7.0 μs. Fig. 5 illustrates a noteworthy association between the LIBS spectral response and the delay time. The peak LIBS signal intensity is observed at approximately 2 μs, suggesting that this specific delay time is optimal for the particular process under consideration.

Optimization of Laser Energy

Optimizing the laser pulse energy is a critical experimental parameter to take into account. Insufficient laser pulse energy results in a weak plasma formation on the sample surface, leading to a decrease in atomic emission intensity. Conversely, when the laser pulse energy is excessively high, the plasma generated becomes overly intense, hindering its ability to achieve local thermodynamic equilibrium. In such a case, a considerable portion of the atomic radiation that has been emitted is reabsorbed by the plasma, resulting in a reduction of the LIBS signal. The excitation energy required for optimal performance varies for each sample matrix, as it is influenced by the material's specific mechanical, thermal, and chemical properties. In our investigation, we undertook an analysis of the dependency of emission intensity on energy for the Ca II 396.84 nm ionic transition line. Our findings show that an energy of 54 mJ/pulse serves as the optimal excitation energy, as represented in Fig. 6.

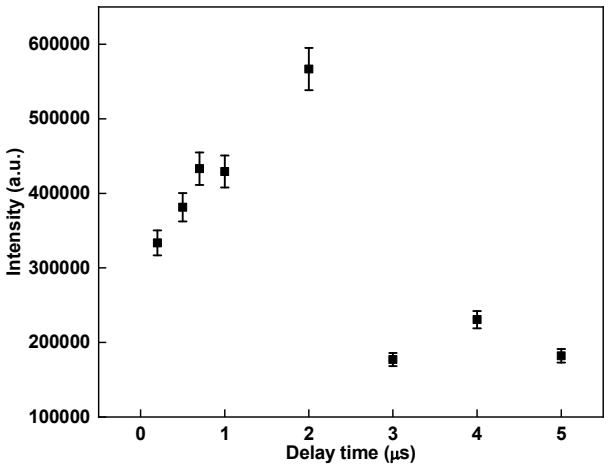

Fig 5. The correlation between LIBS emission intensity and delay time for the Ca II emission line detected at 393.84 nm obtained from tsunami deposit samples

Validation of Local Thermodynamic Equilibrium of Plasma

The key to achieving accurate and consistent qualitative and quantitative analysis of elemental composition and concentration in the test samples lies in maintaining an optically thin and locally thermodynamic equilibrium (LTE) state in the laser-induced plasma formed on the sample surface. Deviation from LTE conditions can result in measurements that are inaccurate and unreliable, primarily due to the occurrence

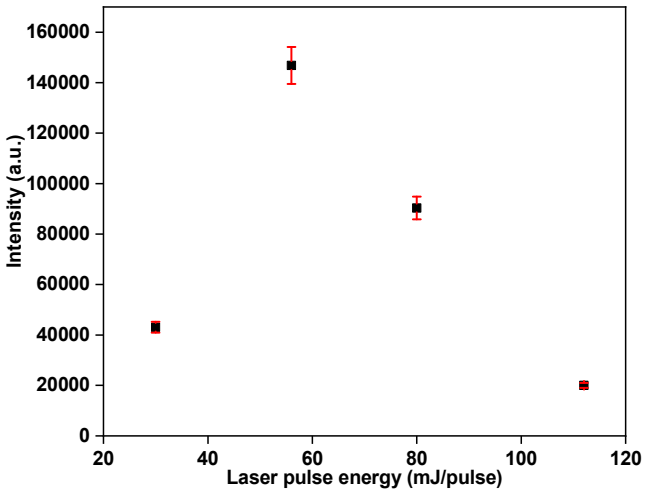

Fig 6. The correlation between LIBS emission intensity and laser energy for the Ca II at 393.84 nm was obtained from tsunami deposit samples

of moderate or strong self-absorption. In contrast, under the conditions of thermodynamic equilibrium, the plasma is regarded as a closed system where all processes within the system achieve equilibrium by balancing their opposing reactions. The generated heat within the system remains confined to it, ensuring that all particles within the plasma, including neutral atoms, ions, radiation, and free electrons, maintain the same temperature. A comprehensive understanding of this system is attained by utilizing a set of equilibrium relations rooted in statistical mechanics. The energy of free electrons is governed by Maxwell distribution the population levels of different excited energy states in neutral atoms or ions are described by the Boltzmann distribution, the population of various ionization stages is elucidated by the Saha-Eggert equation and the energy density of radiation is predicted by Planck function.

Hence, we adopted the Boltzmann plot technique to estimate the plasma temperature by scrutinizing the five Ca emission lines. We engaged the series of intensities for Ca atomic transition lines (I_{ik}), each with its unique transition probabilities (A_{ik}) in conjunction with the degeneracy factor g_k derived from the NIST atomic spectra literature. By assessing the distribution of normalized intensity from a sequence of atomic transition lines of Ca, it becomes plausible to deduce the plasma temperature. The integral line intensity obtained from the measurements corresponds to the transition between the higher energy state E_k and the lower energy state E_i. This transition can be calculated using the Eq. (1) [37].

$$I = FC_s A_{ki} \frac{g_k}{U(T)} \exp\left(\frac{E_k}{kT}\right) \quad (1)$$

In this equation, the constant F represents the experimental parameter, while Cs represents the total number of neutral and ionic elements. The variables A_{ki} and g_k correspond to the transition probabilities from energy level k to i and the statistical weights for the upper energy levels, respectively. Additionally, U(T), E_k, and k symbolize the partition functions, the value of the upper energy levels and the Boltzmann constant of 8.617×10^{-5} eV/k. Upon applying the logarithm to Eq. (1), we derive the following expression (Eq. (2)):

$$\ln\frac{I}{g_k A_{ki}} = -\frac{1}{kT}E_k + \ln\frac{C_s F}{U(T)} \quad (2)$$

Eq. (2) takes on the form of a linear equation, giving rise to the computation of the plasma temperature. The Eq. (2) is used to determine plasma temperature by calculating the slope resulting from the logarithm of intensity for specific elements and their corresponding $g_k A_{ki}$ values. The logarithmic value also exhibits a linear relationship with the upper energy level of the elements under study. Additionally, the y-intercept of the line is directly related to the species' concentration through the constant factor F, offering valuable insights into the sample's characteristics. We utilized a Boltzmann plot curve, exemplified in Fig. 7, to derive the plasma temperature (T) by calculating the slope (m) from plotting the dependent variable against E_i. The resulting plasma temperature can be expressed in either electron volts (eV) or Kelvin (K). Fig. 7 depicts a clear relationship derived from the Ca II emission lines observed in the LIBS spectrum, showcasing the determination of plasma temperature by examining the linear correlation achieved by plotting the logarithm of spectral intensity against the upper energy level. The analysis of slope (−0.849) using Eq. (2) confidently confirms the plasma temperature value in this experiment as 7271 K.

The estimation of electron number density relies on the analysis of Stark broadening occurring in a particular atomic transition line. With an increase in the

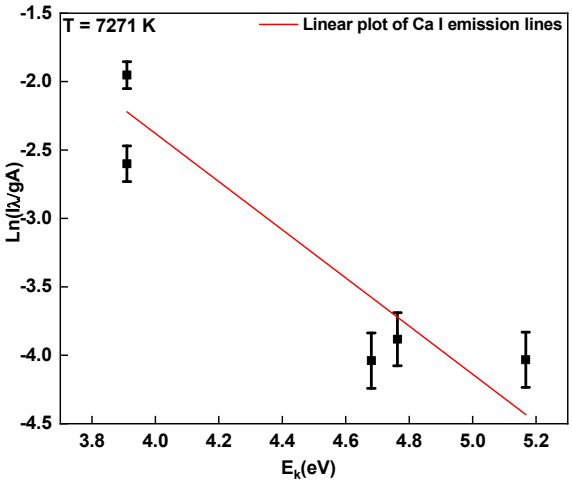

Fig 7. The Boltzmann plot of Ca I emission lines for estimation of plasma temperature

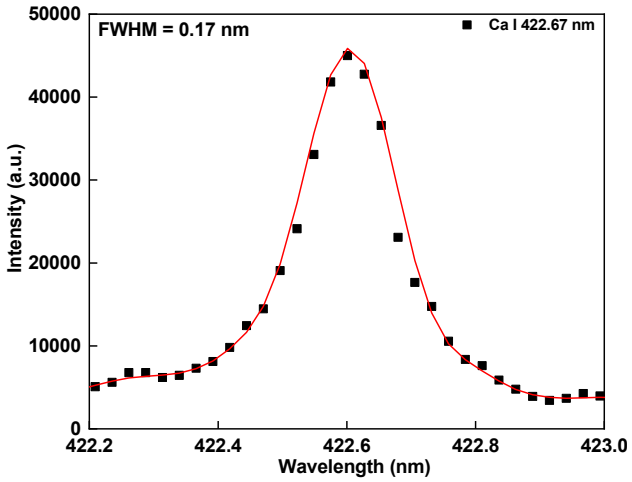

Fig 8. Stark broadening profile of Ca I emission lines (422.67 nm) for determination of electron density

electron number density in the plasma, the electric field within the plasma also rises, leading to a more pronounced Stark broadening phenomenon. Hence, there exists a direct relationship between the electron number density in the plasma and the full-width half maximum (FWHM) of the Stark broadened peak, as explicitly expressed in the Eq. (3):

$$Ne = \left(\frac{\Delta\lambda_{1/2}}{\omega}\right)^{1.478} \times 10^{16}\left(cm^{-3}\right) \quad (3)$$

In this context, $\Delta\lambda_{1/2}$ denotes the FWHM of the studied atomic transition lines, while ω represents the parameter of electron collisions in the plasma. Eq. (3) provides a simple and effective approach for calculating the electron density value using the FWHM peak. In our specific case, the FWHM value of Ca I 422.68 nm was measured at −0.849 nm, as exemplified in Fig. 8.

By inputting this FWHM value for Ca into the equation, we obtained a plasma electron density of 1.7×10^{17} cm^{-3}. It is worth noting that plasma lasers can be considered in a state of LTE if the electron density value meets certain requirements as shown in Eq. (4):

$$Ne \geq 1.6 \times 10^{12}\left(T\right)^{1/2}\left(\Delta\lambda E_{ki}\right)^{3} \quad (4)$$

Furthermore, considering the plasma temperature values and ΔE_{ki} as the largest difference between the two highest energy levels, we derived a threshold value for the electron density on the right-hand side of the equation, resulting in 1.5×10^{17} cm^{-3}. Notably, this value is lower than the actual electron density of 1.7×10^{17} cm^{-3} confirming the fulfilment of Mc-Whriter's criterion. This firmly establishes the plasma system's state of local thermodynamic equilibrium with confidence.

Distinctive Geochemical Markers of the 2004 Indian Ocean Tsunami

We investigated the chemical composition of individual layers of tsunami deposits by capturing their spectra utilizing optimal laser energy and time delay parameters, precisely set at 54 mJ per pulse laser energy and 2 μs delay time. Additionally, we conducted a comprehensive spectral analysis of the sediment samples, covering a wide wavelength range from 200 to 900 nm, to observe the variations among samples collected at various depths (0–32 cm) (Fig. 9).

Significant distinctions were evident between each of the tsunami-deposited and unaffected layers. Terrestrial markers, particularly Fe element, were prominently discernible within the tsunami deposit layer at a depth ranging from 4 to 24 cm. Furthermore, notable heavy metal markers, such as Cu, Cr, Sr, and Co, even at low intensity, were exclusively detected in the tsunami deposit layer, whereas in the non-tsunami layer, these elements remained unobservable. After our investigation, we ascertained unique distinctions in each layer of the tsunami deposits, which were absent in the non-tsunami layer. Most notably, the tsunami sediment bed displayed significantly augmented emission intensities of Mg, Na, K, Ca, Si, V, Mn, Ti, and Ba

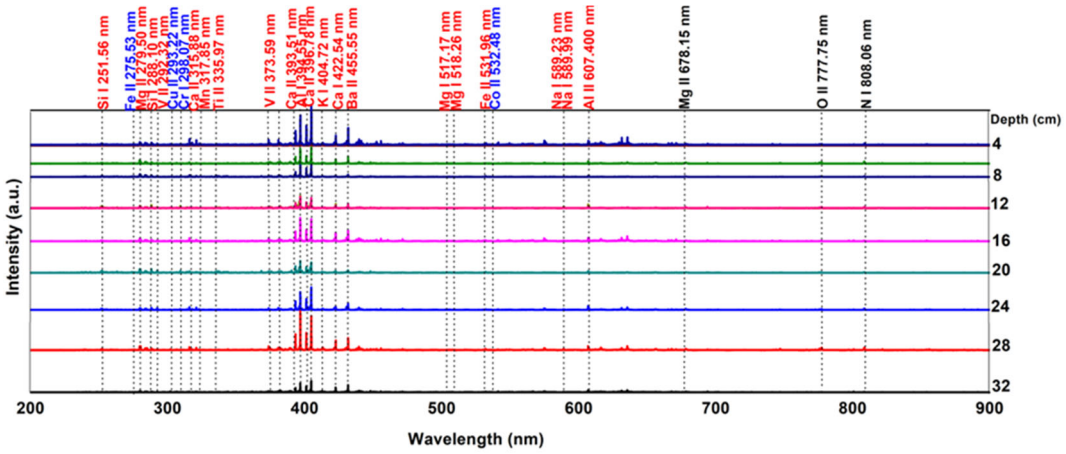

Fig 9. The spectra emission lines of tsunami deposit and non-tsunami deposit samples collected from Seungko Mulat Village were analyzed within the wavelength range of 200–900 nm

Table 1. The atomic and ionic emission lines of the chemical elements obtained in deposit samples collected from Seungko Mulat Village

Elements	Deposit layers	Depth (cm)	Wavelength (nm)
Fe	Topsoil	0–4	254.60, 254.79, 273.90, 274.89, 275.53, 277.67, 283.47, 296.64, 297.26, 314.06, 315.83, 317.87, 320.89, 340.57, 341.78, 401.16
	Tsunami soil	4–24	234.30, 235.73,237.57, 238.17, 238.80, 239.54, 239.90, 283. 17, 294.72, 295.34, 296.64, 297.26, 301.08, 304.66, 305.66, 305.85, 315.83, 319.05, 319.14, 330.59, 341.74, 374.88, 375.79, 376.32, 377.62, 378.95, 379.51, 404.16, 428.89, 442.40, 456.98, 459.65, 505.67, 577.53, 254.60, 254.79, 252.11, 256.29, 258.23, 258.58, 259.79, 259.97, 271.42, 271.85, 273.79, 273.90, 274.89, 275.53, 276.14, 277.67, 278.74, 283.74, 293.62, 301.92, 302.53, 306.59, 314.06, 316.78, 317.87, 320.89, 323.05, 340.57, 580.83, 531.96, 536.37, 541.15, 775.80
	Paleo soil	24–32	254.60, 254.79, 273.90, 274.89, 275.53, 277.67, 296.64, 297.26, 314.06, 315.83, 317.87, 320.89, 340.57, 341.78, 401.16, 401.16, 775.80
Mg	Topsoil	0–4	285.16, 516.62, 517.17, 518.26, 279.50, 280.27
	Tsunami soil	4–24	285.16, 516.62, 517.17, 518.26, 279.50, 280.27
	Paleo soil	24–32	285.16, 516.62, 517.17, 518.26, 279.50, 280.27
Si	Topsoil	0–4	250.72, 251.56, 251.90, 252.37, 252.83, 288.10
	Tsunami soil	4–24	250.72, 251.56, 251.90, 252.37, 252.83, 288.10
	Paleo soil	24–32	250.72, 251.56, 251.90, 252.37, 252.83, 288.10
Ti	Topsoil	0–4	370.54, 342.96, 404.05, 441.17, 452.27, 469.27, 625.81, 626.46, 292.31, 292.77, 334.75, 338.33, 339.27, 398.22, 428.26
	Tsunami soil	4–24	370.54, 342.96, 404.05, 441.17, 452.27, 469.27, 625.81, 626.46, 292.31, 292.77, 334.75. 335.97, 337.17, 338.33, 339.27, 398.22, 428.26
	Paleo soil	24–32	370.54, 342.96, 404.05, 441.17, 452.27, 469.27, 625.81, 626.46, 292.31, 292.77, 334.75, 338.33, 339.27, 398.22, 428.26
Cu	Topsoil	0–4	-
	Tsunami soil	4–24	293.22
	Paleo soil	24–32	-
Cr	Topsoil	0–4	402.25
	Tsunami soil	4–24	293.62, 427.54, 298.07, 402.25, 406.28, 448.91, 450.17
	Paleo soil	24–32	402.25

Elements	Deposit layers	Depth (cm)	Wavelength (nm)
Na	Topsoil	0–4	284,17, 309.20, 588.89, 589.99
	Tsunami soil	4–24	284,17, 309.20, 588.89, 589.99
	Paleo soil	24–32	284,17, 309.20, 588.89, 589.99
Mn	Topsoil	0–4	310.60, 317.85, 342.96
	Tsunami soil	4–24	257.58, 293.87, 310.60, 317.85, 342.96
	Paleo soil	24–32	310.60, 317.85, 342.96
Ba	Topsoil	0–4	455.51
	Tsunami soil	4–24	455.51
	Paleo soil	24–32	455.51
Ca	Topsoil	0–4	315.88, 393.36, 396.84, 422.54
	Tsunami soil	4–24	315.88, 393.36, 396.84, 422.54
	Paleo soil	24–32	315.88, 393.36, 396.84, 422.54
Al	Topsoil	0–4	394.40, 396.15, 606.72, 607.32
	Tsunami soil	4–24	331.45, 394.40, 396.15, 606.72, 607.32
	Paleo soil	24–32	394.40, 396.15, 606.72, 607.32
K	Topsoil	0–4	404.72, 465.93
	Tsunami soil	4–24	404.72, 465.93
	Paleo soil	24–32	404.72, 465.93
W	Topsoil	0–4	344.04, 441.88, 606.36
	Tsunami soil	4–24	344.04, 441.88, 606.36
	Paleo soil	24–32	344.04, 441.88, 606.36
Ni	Topsoil	0–4	-
	Tsunami soil	4–24	772.81, 332.23, 336.57, 451.29, 460.62
	Paleo soil	24–32	772.81
Co	Topsoil	0–4	-
	Tsunami soil	4–24	334.11, 532.48
	Paleo soil	24–32	-
Cd	Topsoil	0–4	-
	Tsunami soil	4–24	298.06
	Paleo soil	24–32	-
V	Topsoil	0–4	289.26, 390.56, 391.16, 448.00, 457.71, 471.37
	Tsunami soil	4–24	289.26, 390.56, 391.16, 448.00, 457.71, 471.37
	Paleo soil	24–32	289.26, 390.56, 391.16, 448.00, 457.71, 471.37
Sr	Topsoil	0–4	421.42, 530.31
	Tsunami soil	4–24	421.42, 530.31
	Paleo soil	24–32	421.42, 530.31
O	Topsoil	0–4	777.19
	Tsunami soil	4–24	777.19
	Paleo soil	24–32	777.19
N	Topsoil	0–4	-
	Tsunami soil	4–24	744.22, 746.83
	Paleo soil	24–32	-

accompanied by prominent emission intensities of organic matter, particularly N and O. These observations provide substantial corroborative evidence of their organic origin, as indicated by the highlighted red indicators. The atomic and ion emission lines of chemical elements obtained from sediment samples

collected from Seungko Mulat Village are presented in Table 1.

To ensure precise observation of each element's spectral line in the sample, we narrowed down the wavelength range incrementally by 10 nm. Notably, within the range of 270–282 nm, distinct emission lines of Fe (271.42, 271.85, 273.79, 273.90, 274.89, 275.53, 276.14, 277.67, and 278.64 nm) and Mg (279.50 and 280.19 nm) were unequivocally identified (Fig. 10(a)). This finding provides robust evidence for the presence of Fe in the tsunami deposits likely attributed to the deposition of hematite (Fe_2O_3) and magnetite (Fe_3O_4) minerals transported by seawater and subsequently settling on land during the tsunami event. Moreover, the intensity of Mg emission in the tsunami sediment layer displayed a gradual reduction with increasing depth. This phenomenon is believed to be a consequence of leaching processes into the underlying sandy soil.

The Si emission line, conspicuously identified at a wavelength of 288.15 nm, assumes a critical role as a significant chemical marker characterizing sandy deposits primarily composed of silicate minerals transported by the force of tsunami waves (Fig. 10(b)) [38]. Analogous to Mg, the highest Si emission intensity was observed in the tsunami deposit layer at a depth of 16 cm. Additionally, within the wavelength range of 330–340 nm, we made a further discovery of four distinct emission lines corresponding to elemental Ti (334.75, 335.97, 337.17, and 338.33 nm) (Fig. 10(c)). It is of utmost importance to emphasize that Ti, alongside Fe, represents a terrestrial resource that serves as a pivotal indicator for discerning heavy mineral deposits transported by the tsunami [39].

Furthermore, our LIBS analysis showcases its proficiency in clearly identifying the presence of salt elements in each stratum of the tsunami deposit. Specifically, emission lines corresponding to elemental salts (Ca and Al) were successfully detected at precise wavelengths of 393.36, 394.40, 396.15, and 396.84 nm (Fig. 10(d)). The emission lines corresponding to elemental K are evident at a wavelength of 404.72 nm (Fig. 11(a)), and two emission lines for Na are observed at wavelengths of 588.99 and 589.59 nm (Fig. 11(b)). The emission intensity of all salt elements exhibited a

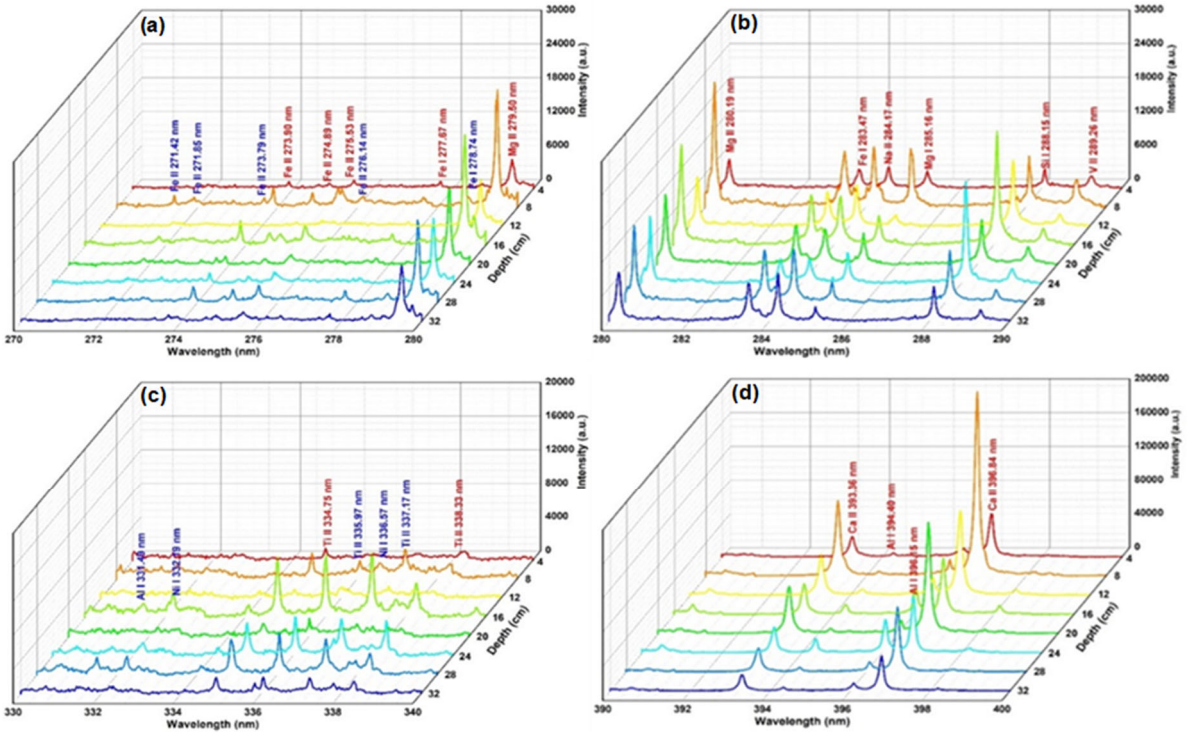

Fig 10. Spectra emission line of tsunami layers and non-tsunami layers from Seungko Mulat Village at wavelength range of (a) 270–280, (b) 280–290, (c) 330–340, and (d) 390–400

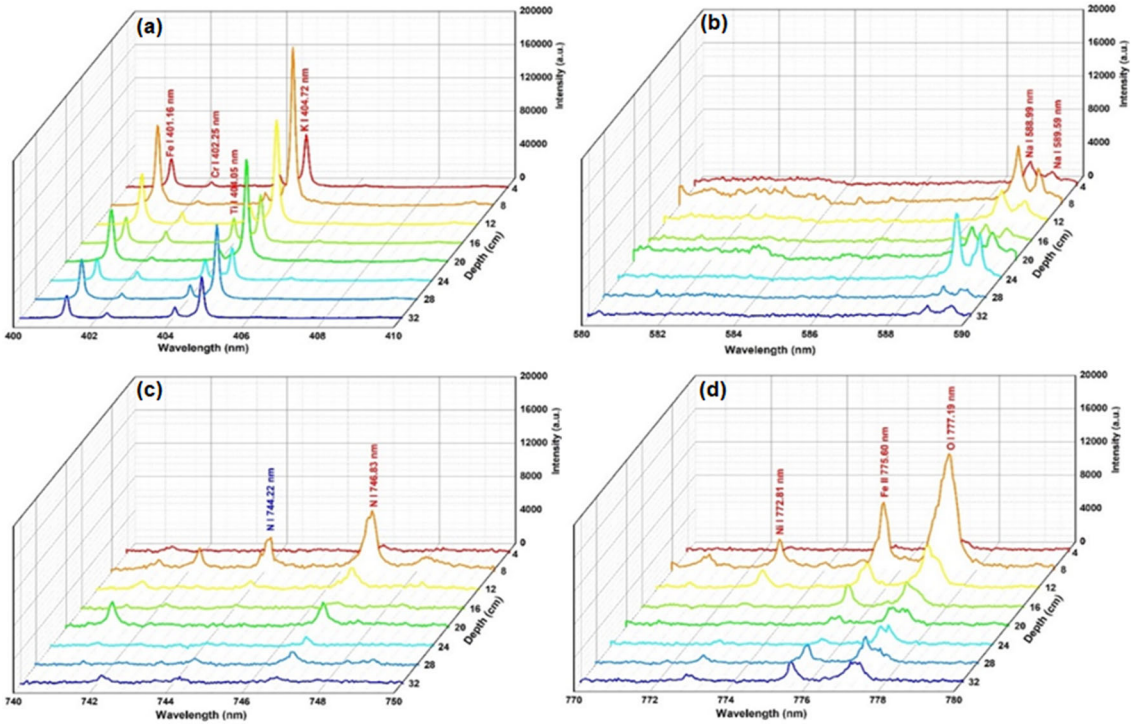

Fig 11. Spectra emission line of tsunami layers and non-tsunami layers from Seungko Mulat Village at a wavelength range of (a) 400–410, (b) 580–590, (c) 740–750, and (d) 770–780 nm

declining trend with increasing depth, and notably, the highest emission intensity was observed at a depth of 4 cm. The higher concentrations of salt components, such as Ca, Mg, K, and Na are commonly encountered in tsunami deposits and have been widely utilized as indicators of seawater presence, thus aiding in distinguishing tsunami deposits [9]. Elemental Ca, for instance, originates from marine carbonate ($CaCO_3$), which is biogenic formed by marine organisms. Elemental Na can be sourced from sea salt and feldspar minerals, and these elements can generally be well-preserved for over 2000 years in tsunami sediments, although some Na may have been leached away due to heavy rainfall [5]. The presence of elemental salts (Ca, Mg, Na, and K) in tsunami deposits can be readily identified due to their higher intensity compared to other chemical elements. In addition to terrestrial markers, heavy metal elements, and salt components, the application of the LIBS technique in this study facilitated the detection of emission lines corresponding to organic elements, namely N and O, in all analyzed samples of tsunami deposits. Two emission lines associated with element N were identified at wavelengths of 744.22 and 746.83 nm (Fig. 11(c)), while the emission line linked to element O was observed at a wavelength of 777.19 nm (Fig. 11(d)).

To strengthen the findings obtained from LIBS analysis, we conducted a comparative evaluation with the results obtained from XRF measurements (Table 2). The XRF analysis results indicate that the topsoil layer, the 2004 Indian Ocean tsunami layer, and the paleo soil layer contain Ca, K, Mg, Na, Al, Si, Fe, Ti, Sr, Mn, Cl, and S. Our analysis confirms that both techniques, LIBS and XRF, are capable of detecting various chemical elements, including Ca, K, Mg, Na, Al, Si, Fe, Ti, Sr, and Mn. However, it is worth noting that certain elements, namely O, N, Ba, Cu, Cr, Pb, Ni, V, Zr, P, and S, exhibit unique characteristics exclusively observed through either LIBS or XRF methodologies. In particular, LIBS outperforms XRF specifically due to its ability to analyze nearly all elements simultaneously and detect light elements (O, N), as well as certain heavy metals (Ba, Cu, Cr, Co, Cd, Pb, Ni, V, and W) beyond the detection limits of XRF. Although XRF is recognized as a conventional technique for rapid elemental identification,

Table 2. The comparative results of LIBS and XRF techniques for the elements present in deposit samples from Seungko Mulat Village

LIBS	XRF
Ca	Ca
K	K
Mg	Mg
Na	Na
Al	Al
Si	Si
Fe	Fe
Ti	Ti
Ba	Sr
Sr	Mn
Cu	Cl
Cr	S
Co	
Cd	
W	
Pb	
Mn	
Ni	
V	
O	
N	

it is important to note that not all elements are easily detected using XRF techniques.

XRF faces difficulty in detecting chemical components with low molecular weights due to the technical characteristics of the method. XRF utilizes X-rays to analyze samples and detect chemical elements based on the characteristic X-ray radiation produced by atoms in the sample after being exposed to X-rays. However, elements with low molecular weights exhibit weak X-ray radiation characteristics, making them challenging to detect with high sensitivity by XRF. Additionally, in the detection of elements with low molecular weights, interference from other elements in the sample can also be a problem, reducing the accuracy and reliability of the analysis results. In contrast, LIBS operates by subjecting the sample to an intense laser pulse, triggering plasma formation on its surface. This process ionizes and energizes the atoms within the sample. The resulting plasma reaches exceedingly high temperatures, causing all elements within the sample to ionize and emit electromagnetic radiation, encompassing X-rays, ultraviolet, and visible light. Subsequently, this emitted radiation is scrutinized to discern the constituent elements of the sample. The paramount advantage of LIBS in detecting low-molecular-weight elements lies in the plasma's elevated temperature, which facilitates the ionization and excitation of atoms, even those with low molecular weights. Furthermore, the LIBS technique can generate rich spectra of various elements in a short period, making it highly suitable for rapid and sensitive chemical analysis, including for light elements, which presents a challenge for detection using other conventional analytical techniques.

In the context of earlier discussions, the presence and relative abundance of Mg, Ca, and K content emerge as pivotal indicators to authenticate the incursion of inland seawater. The discernible disparity in carbonate concentrations between seawater and freshwater or terrestrial environments renders these elements valuable geochemical proxies. However, certain geological settings, such as the Mangaia in Cook Islands introduce an intriguing twist [40]. Here, geochemical markers Ca and Sr are primarily derived from freshwater gastropod shells, necessitating a nuanced approach to interpretation. This phenomenon is attributed to the influx of terrestrial sediments into the lagoon, effectively concealing the characteristic seawater signal. It is essential to recognize that the composition and concentration of elements in stratigraphy can display considerable variations, imparting a formidable challenge in differentiating between markers of seawater and freshwater. As a consequence, researchers have turned to the comparative analysis of chemical element concentrations to identify marine sediments that have infiltrated terrestrial environments. Notably, normalized Ti and Si values have emerged as widely adopted geochemical proxies to detect tsunami and paleo-tsunami deposits [20]. Moreover, preceding studies have employed LIBS emission intensity ratios to characterize tsunami sediment samples. In this study, we undertake a comprehensive assessment of the emission intensity ratios derived from LIBS analysis to

characterize the tsunami deposit samples. We assessed a diverse array of emission intensity ratios, encompassing Mg/Ti, Ba/Ti, Si/Ti, Pb/Ti, K/Ti, Al/Ti, Ca/Fe, Ca/Mg, and Ca/K, which provides distinct characteristics to individual layers of the tsunami deposits (Tables 3 and 4).

Through the examination of a series of emission intensity ratios for various elements at different depths, our results indicate that the highest element emission intensity ratios are present in the tsunami deposit layers, particularly at a depth of 12 cm. Prior studies have demonstrated that following the 2011 Tohoku tsunami, soil samples collected from the Sendai plains, Tohoku, Japan, exhibited a significant increase in the Na/Ti concentration ratio, surpassing the ratio in the unaffected area [8]. Specifically, in this study, the Na/Ti ratio was found to be two times higher in the tsunami sediment layer (at 4) at a depth of 12 cm compared to the topsoil and an impressive 13 times higher than in the paleo soil layer (Table 3). Moreover, previous investigations have indicated that the Ca/Ti ratio can serve as an indicator of the presence of $CaCO_3$, particularly associated with shell hash or bioclast fractions in samples, enabling comparisons between seawater signals and terrestrial markers. In this study,

Table 3. LIBS emission intensity ratios of chemical elements detected in sediment samples collected from Seungko Mulat Village at depths of 0–32 cm for Na/Ti, Ca/Ti, Mg/Ti, Ba/Ti, Si/Ti, and Fe/Ti

Depth of deposits (cm)	LIBS intensity emission ratio						Remarks
	Na/Ti (nm)	Ca/Ti (nm)	Mg/Ti (nm)	Ba/Ti (nm)	Si/Ti (nm)	Fe/Ti (nm)	
	Na I	Ca II	Mg I	Ba I	Si I	Fe I	
	588.85	396.78	279.50	455.55	288.10	283.44	
	Ti I	Ti I	Ti I	Ti I	Ti I	Ti I	
	337.75	337.75	337.75	337.75	337.75	337.75	
4	2.0	48.0	4.0	3.0	3.0	3.0	Topsoil
8	2.0	88.0	8.0	5.0	3.0	4.0	
12	4.0	128.0	11.0	5.0	15.0	7.0	
16	0.4	16.0	4.0	0.5	5.0	2.0	
20	2.0	102.0	10.0	2.0	6.0	5.0	
24	2.0	16.0	3.0	0.5	5.0	1.0	
28	0.3	19.0	3.0	1.0	2.0	2.0	Paleo soil
32	0.6	24.0	5.0	1.0	3.0	3.0	Paleo soil

Table 4. LIBS emission intensity ratios of chemical elements detected in sediment samples collected from Seungko Mulat Village at depths of 0–32 cm for K/Ti, Al/Ti, Ca/Fe, Ca/Mg, and Ca/K

Depth of deposits (cm)	LIBS intensity emission ratio					Remarks
	K/Ti (nm)	Al/Ti (nm)	Ca/Fe (nm)	Ca/Mg (nm)	Ca/K (nm)	
	K I	Al II	Ca II	Ca II	Ca II	
	404.72	395.44	396.78	396.78	396.78	
	Ti I	Ti I	Fe I	Mg I	K I	
	337.75	337.75	283.44	279.50	404.72	
4	63.0	3.0	17.0	11.0	1.0	Topsoil
8	76.0	1.0	24.0	11.0	1.0	
12	164.0	7.0	19.0	13.0	1.0	
16	14.0	3.0	8.0	4.0	1.0	
20	95.0	3.0	19.0	10.0	1.0	
24	11.0	4.0	15.0	5.0	1.0	
28	28.0	1.0	9.0	6.0	1.0	Paleo soil
32	30.0	1.0	7.0	5.0	1.0	Paleo soil

the Ca/Ti, Mg/Ti, and K/Ti ratios were observed to be approximately three times higher than the ratios found in the topsoil, with a value of 128, 11, and 164, respectively (Tables 3 and 4). Additionally, a remarkable increase in the Si/Ti ratio was identified, displaying values approximately five times higher (at 15) than those observed in the unaffected subsoil (Table 3).

The presence of Mg^{2+} serves as a robust indicator for assessing the tsunami impact in the Sound of Lefkada, Greece, while the limnic and terrestrial markers demonstrate a diminished Ca concentration ratio [41]. However, in this study, the ratios of Ca/Mg, Ca/K, and Ca/Fe in both the tsunami sediment layer and the non-tsunami layer did not exhibit significant differences, suggesting that this ratio is not suitable for identifying tsunami geochemical markers in this particular region. Nonetheless, the emission intensity ratios of Ca/Ti, Si/Ti, and K/Ti in tsunami deposits exhibited significantly different values compared to the non-tsunami layer. Therefore, these ratios can be proposed as geochemical indicators for identifying the deposit samples related to the 2004 Indian Ocean tsunami in our study. Our findings are consistent with previous studies, which identified soil affected by the 2004 Indian Ocean tsunami in Aceh Province based on the elevated intensity values of the Si/Ti ratio [2,16-17].

PCA

We embarked on an investigation into the potential for cluster formation by applying the PCA algorithm to the LIBS data. Our focal point revolved around the comprehensive analysis of the distinctive characteristics exhibited by tsunami deposits and non-tsunami layers. Our approach involved generating 2D PCA scores adeptly harnessing LIBS spectra spanning various wavelength ranges, specifically 200–900, 200–550, and 551–900 nm, as illustrated in Fig. 12. Regrettably, the PCA score plot rendered within these extensive wavelength ranges yielded indistinct separation patterns indicating a suboptimal performance in discriminating between the intriguing realms of tsunami and non-tsunami deposit samples. This lack of clear differentiation could be attributed to the relatively analogous chemical compositions prevalent within the tsunami sediment layer and non-tsunami layer. Furthermore, we performed LIBS spectral PCA with wavelength increments of 100 nm. Regrettably, the outcomes remained unsatisfactory, characterized by dispersed data points representing the tsunami and non-tsunami layers, rendering it unsuitable for the discrimination of tsunami deposit layers (Fig. 12).

In pursuit of refining our analytical approach, we opted for a more fine-grained wavelength resolution, narrowing the range to increments of 10 to 15 nm. Within this constrained domain, we conducted LIBS-PCA analyses within the wavelength range of 270–285 and 580–590 nm, where elements Fe, Mg, and Na demonstrated conspicuous intensities. However, despite this focused effort, the results remained less than satisfactory, displaying inaccuracies. Through our meticulous exploration of alternate wavelength ranges, we made a fascinating discovery that the tsunami deposits

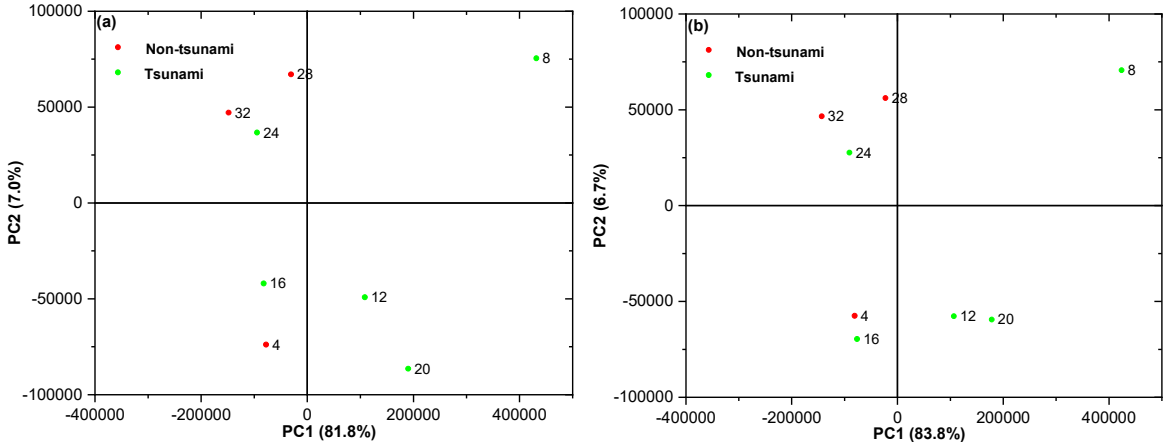

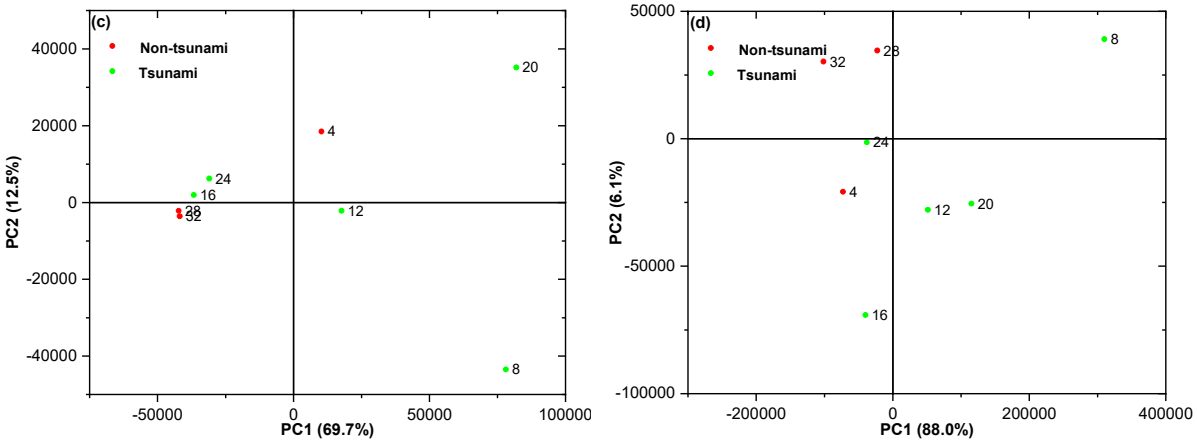

Fig 12. LIBS-PCA plot of deposit samples in the wavelength ranges of (a) 200-900, (b) 200-550, (c) 551-900, and (d) 300-400 nm

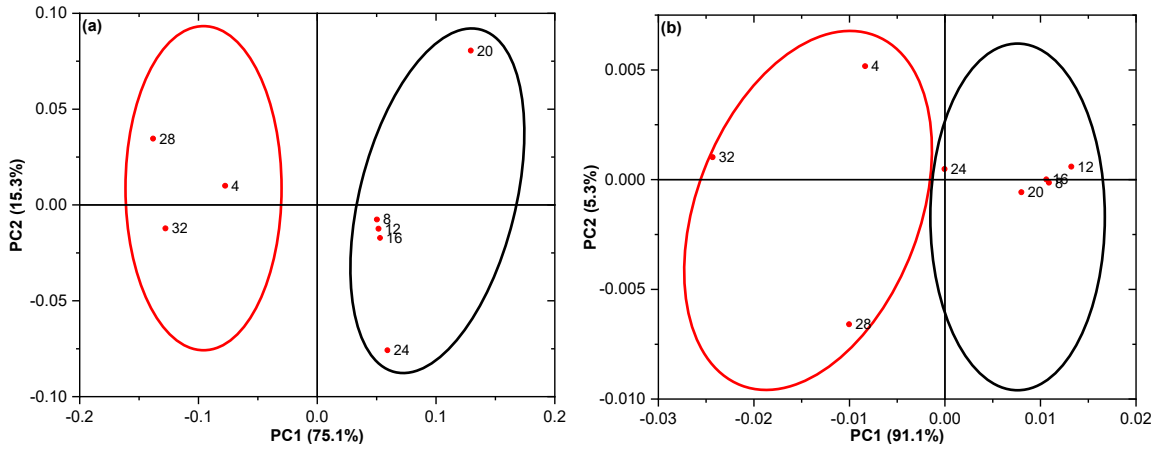

Fig 13. LIBS PCA plot of deposit samples at the wavelength range of (a) 330–340 nm and (b) 390–405 nm

and non-tsunami layers formed distinct and discernible clusters in the PCA score plot when generated within the 330–340 and 390–405 nm wavelength domains (Fig. 13).

Notably, these specific ranges are precisely aligned with the emission lines of inorganic elements Ti, Ca, Al, K, and Na. The ensuing PC1 values, namely 87 and 85% for the respective wavelength ranges, provided compelling evidence that the sedimentary tsunami deposits and non-tsunami layers in our study can be effectively differentiated based on the elemental composition of Ti, Ca, Al, K, and Na in the samples. Remarkably, no data smoothing was applied within this particular wavelength range, underscoring the robustness of our conclusions.

■ CONCLUSION

We have developed and optimized a LIBS system to conduct layer-by-layer chemical profiling of sediment samples collected from Seungko Mulat, an area impacted by the 2004 Indian Ocean tsunami, situated on the coast of Aceh Besar district. The 2004 Indian Ocean tsunami deposit exhibited clear terrestrial markers and heavy metal indicators, accompanied by a significant intensification in the atomic emission lines of numerous metal elements and organic components, thereby distinctly differentiating it from both the topsoil and paleosoil layers. The emission intensity ratios, particularly Ca/Ti, Si/Ti, and K/Ti, exhibit unique values exclusively within the sediment layer impacted by the 2004 Indian Ocean tsunami, registering at 128, 15, and 164, respectively. These distinctive values underscore their potential as robust geochemical markers, essential for elucidating the dynamics of the 2004 Indian Ocean tsunami inundation in Seungko

Mulat Village. Employing LIBS-PCA analysis, spectral lines associated with inorganic elements, including Ti, Ca, Al, Fe, and K, play a pivotal role in effectively distinguishing between sediment layers influenced by the 2004 Indian Ocean tsunami and those unaffected (topsoil and paleosoil). This study contributes valuable insights for further research by establishing strong geochemical markers to differentiate between the 2004 Indian Ocean tsunami deposits and unaffected sedimentation layers, advancing analytical techniques through the development of LIBS for layer-by-layer chemical profiling, and supporting the development of effective disaster management strategies for tsunami-prone coastal areas.

■ ACKNOWLEDGMENTS

The authors express their gratitude for the financial support received from the Directorate of Research and Community Service, Directorate General of Research Strengthening and Development, Ministry of Research, Technology, and Higher Education, Government of the Republic of Indonesia through the Research of Master to Doctoral Education for Excellent Undergraduate (*Program Magister Doktor Sarjana Unggulan* PMDSU) 2020 under contract number: 111/UN11.2.1/PT.01.03/DPRM/2020 on August 4, 2020.

■ CONFLICT OF INTEREST

The authors affirm that they do not have any conflicts of interest.

■ AUTHOR CONTRIBUTIONS

Rara Mitaphonna contributed to the sampling, collection, and processing of LIBS data and the drafting of the manuscript. Muliadi Ramli assisted in data analysis, offering critical insights into the existing findings. Nazli Ismail played in field data collection and provided invaluable input for interpreting the geological context. Nasrullah Idris facilitated the retrieval of LIBS spectral data and offered profound insights into the geochemical implications of the analysis results.

■ REFERENCES

[1] Ratnayake, A.S., Wijewardhana, T.D.U., Haraguchi, T., Goto, K., Ratnayake, N.P., Tetsuka, H., Yokoyama, Y., Miyairi, Y., and Attanayake, A.M.A.N.B., 2023, Sedimentological observations and geochemical characteristics of paleo-tsunami deposits along the east coast of Sri Lanka in the Indian Ocean, *Quat. Int.*, 661, 49–59.

[2] Idris, N., Gondal, M.A., Lahna K., Ramli, M., Sari, A.M., Aldakheel, R.K., Mitaphonna, R., Dastageer, M.A., Kurihara, K., Kurniawan, K.H., and Almesserie, M.A., 2022, Geochemistry study of soil affected catastrophically by tsunami disaster triggered by 2004 Indian Ocean earthquake using a fourth harmonics (λ = 266 nm) Nd:YAG laser induced breakdown spectroscopy, *Arabian J. Chem.*, 15 (7), 103847.

[3] Daly, P., Halim, A., Nizamuddin, N., Ardiansyah, A., Hundlani, D., Ho, E., and Mahdi, S., 2017, Rehabilitating coastal agriculture and aquaculture after inundation events: Spatial analysis of livelihood recovery in post tsunami Aceh, Indonesia, *Ocean Coastal Manage.*, 142, 218–232.

[4] Rubin, C.M., Horton, B.P., Sieh, K., Pilarczyk, J.E., Daly, P., Ismail, N., and Parnell, A.C., 2017, Highly variable recurrence of tsunamis in the 7.400 years before the 2004 Indian Ocean tsunami, *Nat. Commun.*, 8 (1), 16019.

[5] Watanabe, T., Tsuchiya, N., Yamasaki, S., Sawai, Y., Hosoda, N., Nara, F.W., Nakamura, T., and Komai, T., 2020, A geochemical approach for identifying marine incursions: Implications for tsunami geology on the Pacific coast of northeast Japan, *Appl. Geochem.*, 118, 104644.

[6] Chagué-Goff, C., Szczuciński, W., and Shinozaki, T., 2017, Applications of geochemistry in tsunami research, A review, *Earth-Sci. Rev.*, 165, 203–244.

[7] Sawai, Y., Namegaya, Y., Tamura, T., Nakashima, R., and Tanigawa, K., 2015, Shorter intervals between great earthquakes near Sendai: Scour ponds and a sand layer attributable to A.D. 1454 overwash, *Geophys. Res. Lett.*, 42 (12), 4795–4800.

[8] Pilarczyk, J.E., Sawai, Y., Namegaya, Y., Tamura, T., Tanigawa, K., Matsumoto, D., Shinozaki, T., Fujiwara, O., Shishikura, M., Shimada, Y., Dura, T., Horton, B.P., Parnell, A.C., and Vane, C.H., 2021, A

further source of Tokyo earthquakes and Pacific Ocean tsunamis, *Nat. Geosci.*, 14 (10), 796–800.

[9] Shinozaki, T., 2021, Geochemical approach in tsunami research: Current knowledge and challenges, *Geosci. Lett.*, 8 (1), 6.

[10] Shinozaki, T., Sawai, Y., Ikehara, M., Matsumoto, D., Shimada, Y., Tanigawa, K., and Tamura, T., 2022, Identifying tsunami traces beyond sandy tsunami deposits using terrigenous biomarkers: A case study of the 2011 Tohoku-oki tsunami in a coastal pine forest, northern Japan, *Prog. Earth Planet. Sci.*, 9 (1), 29.

[11] Paris, R., Sabatier, P., Biguenet, M., Bougouin, A., André, G., and Roger, J., 2021, A tsunami deposit at Anse Meunier, Martinique Island: Evidence of the 1755 CE Lisbon tsunami and implication for hazard assessment, *Mar. Geol.*, 439, 106561.

[12] Yamada, M., Fujino, S., Chiba, T., Chagué, C., and Takeda, D., 2021, Recurrence of intraplate earthquakes inferred from tsunami deposits during the past 7300 years in Beppu Bay, southwest Japan, *Quat. Sci. Rev.*, 259, 106901.

[13] Gouramanis, C., Switzer, A.D., Jankaew, K., Bristow, C.S., Pham, D.T., and Ildefonso, S.R., 2017, High-frequency coastal overwash deposits from Phra Thong Island, Thailand, *Sci. Rep.*, 7 (1), 43742.

[14] Syamsidik, S., Al'ala, M., Fritz, H.M., Fahmi, M., and Hafli, T.M., 2019, Numerical simulations of the 2004 Indian Ocean tsunami deposits' thicknesses and emplacements, *Nat. Hazards Earth Syst. Sci.*, 19 (6), 1265–1280.

[15] Mitaphonna, R., Ramli, M., Ismail, N., Kurihara, K., Subianto, M., Gondal, M.A., and Idris, N., 2021, Preliminary evaluation of chemical component in the 2004 Indian Ocean giant tsunami impacted soil using CO_2 laser-induced breakdown spectroscopy (LIBS), *J. Phys.: Conf. Ser.*, 1816 (1), 1012035.

[16] Mitaphonna, R., Ramli, M., Ismail, N., and Idris, N., 2023, Evaluation of geochemical signature in soil sampled from a 2004 Indian Ocean tsunami-stricken region in Aceh Province located in the western part of Indonesia using scanning electron microscopy–energy dispersive X-ray (SEM-EDX) spectroscopy and its compatibility with X-ray fluorescence (XRF) measurement, *Philipp. J. Sci.*, 152 (1), 485–499.

[17] Mitaphonna, R., Ramli, M., Ismail, N., Lahna, K., and Idris, N., 2023, X-ray fluorescence (XRF) investigation of soil sample from 2004 Indian Ocean tsunami affected region in Aceh of Indonesia, *AIP Conf. Proc.*, 2858 (1), 050001.

[18] Moreira, S., Costa, P.J.M., Andrade, C., Ponte Lira, C., Freitas, M.C., Oliveira, M.A., and Reichart, G.J., 2017, High resolution geochemical and grain-size analysis of the AD 1755 tsunami deposit: Insights into the inland extent and inundation phases, *Mar. Geol.*, 390, 94–105.

[19] Costa Ferreira, S.L., dos Anjos, J.P., Assis Felix, C.S., da Silva Junior, M.M., Palacio, E., and Cerda, V., 2019, Speciation analysis of antimony in environmental samples employing atomic fluorescence spectrometry – Review, *TrAC, Trends Anal. Chem.*, 110, 335–343.

[20] Ayyıldız, M.F., Yazıcı, E., Şaylan, M., Chormey, D.S., and Bakırdere, S., 2021, Determination of copper in human blood serum by flame atomic absorption spectrometry after UV-assisted Fenton digestion using binary magnetite nanoparticles, *Measurement*, 186, 110108.

[21] Xu, J., Guo, Y., Yang, S., Hohl, S.V., and Zhang, W., 2022, Reliable determination of SiO_2 concentrations in sediments via sequential leaching and ICP-OES/MS analysis, *J. Geochem. Explor.*, 242, 107090.

[22] Ravansari, R., Wilson, S.C, and Tighe, M., 2020, Portable X-ray fluorescence for environmental assessment of soils: Not just a point-and-shoot method, *Environ. Int.*, 134, 105250.

[23] Al-Musawi, M., and Kaczmarek, S., 2020, A new carbonate-specific quantification procedure for determining elemental concentrations from portable energy-dispersive X-ray fluorescence (PXRF) data, *Appl. Geochem.*, 113, 104491.

[24] Cremers, D.A., and Chinni, R.C., 2009, Laser-induced breakdown spectroscopy capabilities and limitations, *Appl. Spectrosc. Rev.*, 44 (6), 457–506.

[25] Brunnbauer, L., Gajarska, Z., Lohninger, H., and Limbeck, A., 2023, A critical review of recent trends

in sample classification using Laser-Induced Breakdown Spectroscopy (LIBS), *TrAC, Trends Anal. Chem.*, 159, 116859.

[26] Gaft, M., Nagli, L., Gornushkin, I., and Raichlin, Y., 2020, Review on recent advances in analytical applications of molecular emission and modelling, *Spectrochim. Acta, Part B*, 173, 105989.

[27] Villas-Boas, P.R., Franco, M.A., Martin-Neto, L., Gollany, H.T., and Milori, D.M.B.P., 2020, Applications of laser-induced breakdown spectroscopy for soil characterization, part II: Review of elemental analysis and soil classification, *Eur. J. Soil Sci.*, 71 (5), 805–818.

[28] Lin, P., Wen, X., Ma, S., Liu, X., Xiao, R., Gu, Y., Chen, G., Han, Y., and Dong, D., 2023, Rapid identification of the geographical origins of crops using laser-induced breakdown spectroscopy combined with transfer learning, *Spectrochim. Acta, Part B*, 206, 106729.

[29] Tavares, T.R., Mouazen, A.M., Nunes, L.C., dos Santos, F.R., Melquiades, F.L., da Silva, T.R., Krug, F.J., and Molin, J.P., 2022, Laser-Induced Breakdown Spectroscopy (LIBS) for tropical soil fertility analysis, *Soil Tillage Res.*, 216, 105250.

[30] Idris, N., Ramli, M., Khumaeni, A., and Kurihara, K., 2018, Detection of salts in soil using transversely excited atmospheric (TEA) carbon dioxide (CO_2) laser-induced breakdown spectroscopy (LIBS) by the aid of a metal mesh, *J. Phys.: Conf. Ser.,* 1011 (1), 012055.

[31] Kelsey, H.M., Engelhart, S.E., Pilarczyk, J.E., Horton, B.P., Rubin, C.M., Daryono, M.R., Ismail, N., Hawkes, A.D., Bernhardt, C.E., and Cahill, N., 2015, Accommodation space, relative sea level, and the archiving of paleo-earthquakes along subduction zones, *Geological*, 43 (8), 675–678.

[32] Folk, R.L., and Ward, W.C., 1957, Brazos River bar [Texas]; A study in the significance of grain size parameters, *J. Sediment. Res.*, 27 (1), 3–26.

[33] Blott, S.J., and Pye, K., 2001, GRADISTAT: A grain size distribution and statistics package for the analysis of unconsolidated sediments, *Earth Surf. Processes Landforms*, 26 (11), 1237–1248.

[34] Hong, I., Dura, T., Ely, L.L., Horton, B.P., Nelson, A.R., Cisternas, M., Nikitina, D., and Wesson, R.L., 2017, A 600-year-long stratigraphic record of tsunamis in south-central Chile, *Holocene*, 27 (1), 39–51.

[35] Mitaphonna, R., Ramli, M., Ismail, N., Hartadi, B.S., and Idris, N., 2023, Identification of possible preserved 2004 Indian Ocean tsunami deposits collected from Pulot Village in Aceh Besar Regency, Indonesia, *J. Phys.: Conf. Ser.*, 2582 (1), 012033.

[36] Bellanova, P., Frenken, M., Reicherter, K., Jaffe, B., Szczuciński, W., and Schwarzbauer, J., 2020, Anthropogenic pollutants and biomarkers for the identification of 2011 Tohoku-oki tsunami deposits (Japan), *Mar. Geol.*, 422, 106117.

[37] Ciucci, A., Palleschi, V., Rastelli, S., Salvetti, A., Singh, D.P., and Tognoni, E., 1999, CF-LIPS: A new approach to LIPS spectra analysis, *Laser Part. Beams*, 17 (4), 793–797.

[38] Yu, N.T., Yen, J.Y., Chen, W.S., Yen, I.C., and Liu, J.H., 2016, Geological records of western Pacific tsunamis in northern Taiwan: AD 1867 and earlier event deposits, *Mar. Geol.*, 372, 1–16.

[39] Watanabe, T., Kagami, S., and Niwa, M., 2022, Geochemical and heavy mineral signatures of marine incursions by a paleotsunami on the Miyazaki plain along the Nankai–Suruga trough, the Pacific coast of southwest Japan, *Mar. Geol.*, 444, 106704.

[40] Chagué-Goff, C., Chan, J.C.H., Goff, J., and Gadd, P., 2016, Late Holocene record of environmental changes, cyclones and tsunamis in a coastal lake, Mangaia, Cook Islands, *Isl. Arc*, 25 (5), 333–349.

[41] Vött, A., Brückner, H., Brockmüller, S., Handl, M., May, S.M., Gaki-Papanastassiou, K., Herd, R., Lang, F., Maroukian, H., Nelle, O., and Papanastassiou, D., 2009, Traces of Holocene tsunamis across the Sound of Lefkada, NW Greece, *Global Planet. Change*, 66 (1-2), 112–128.